photonics

MDPI

Article

Polarization-Sensitive Structural Colors Based on Anisotropic Silicon Metasurfaces

Xiao Shang [1,2], Jiebin Niu [1,2], He Li [1,2], Longjie Li [1,2], Huakui Hu [1,2], Cheng Lu [1] and Lina Shi [1,*]

[1] State Key Lab of Fabrication Technologies for Integrated Circuits, Institute of Microelectronics of the Chinese Academy of Sciences, No. 3 West Road, Beitucheng, Beijing 100029, China; shangxiao@ime.ac.cn (X.S.)
[2] University of Chinese Academy of Sciences, 19 Yuquan Road, Shijingshan District, Beijing 100049, China
* Correspondence: shilina@ime.ac.cn

Abstract: Structural colors based on all-dielectric metasurfaces hold great promise for a wide range of applications, including high-density optical storage, ultra-high-resolution 3D displays, imaging security certification, and so on. However, achieving dynamic tunable structural color with a compact and simple Si platform remains a great challenge. Here, we propose a dynamic tunable structural coloration with polarization-sensitive metasurfaces consisting of arrays of Si elliptical nanopillars, enabling full-colored images to be displayed and switched through the control of the polarization of incident light. A distinct feature of our design is that the color phase is independent of the viewing angle, which is fundamental for real applications. Moreover, we demonstrated that dual and multiple colors can be obtained by varying the angle of either the polarizer or the analyzer. Our scheme provides a simple yet general approach for potential applications in the fields of virtual reality, ultra-high-resolution 3D displays, and high-density information storage.

Keywords: structural color; metasurface; Si nanostructures; polarization

Citation: Shang, X.; Niu, J.; Li, H.; Li, L.; Hu, H.; Lu, C.; Shi, L. Polarization-Sensitive Structural Colors Based on Anisotropic Silicon Metasurfaces. *Photonics* **2023**, *10*, 448. https://doi.org/10.3390/photonics10040448

Received: 17 March 2023
Revised: 3 April 2023
Accepted: 10 April 2023
Published: 13 April 2023

1. Introduction

Color, the main visual vehicle for human perception of the real world, is a visual perception of light generated by the eye, brain, and life experience [1,2]. Visible light is reflected or absorbed by objects, which can produce different colors and bring us a colorful world [3,4]. Although chemical pigments have many applications in industrial products, it has obvious drawbacks: they cannot endure durative high-temperature or high-intensity illumination, and they threaten the environment and human health [5]. Additionally, these pigments have spots that are around 25 nm, which leads to a low resolution of less than 1000 dpi. It is difficult to meet the permanence of coloring and, most importantly, the low resolution of the colors produced by these conventional dyes and pigments limits their practical application in advanced color displays and high-resolution images. By contrast, structural colors offer an alternative coloring mechanism that is physically derived from the controlled scattering, diffraction, and interference of light through nanostructures or microstructures [6–13]. It is known that the Mie resonances appear when the incident electromagnetic wave is comparable to the physical dimension of the resonator for high-index dielectric nanostructures [14,15]. Thus, vibrant colors can be obtained by simply tuning the structural parameters rather than relying on their chemical nature, holding potential for diverse applications, such as high-resolution color printings [16–33], high-resolution digital displays [10,34–37], focusing hyperlens or holographic hyperlens [38–40], and information storage [41,42].

Although some typical configurations, such as nanoparticles, nanogratings, and multi-layer thin films have been utilized to generate highly saturated and pure structural colors, the practical applications of structural color in data storage, optical security, and optical steganography are still restricted because most systems can only generate static colors. In order to overcome these limitations, more scholars began to work on polarization-tunable

anisotropic nanostructures and actively tunable metasurface [43–62]. For instance, Olson et al. modulated the brightness of color by incorporating aluminum nanorod array pixels into a liquid crystal display with an applied voltage [36], Xu et al. demonstrated fast monochromatic and full-color electrochromic switching using electrochromic polymer nanoslit arrays [63]. However, the incomplete full-color spectral response and complicated electrical device structures significantly hinder their practical application. Hence, challenges remain in simultaneously achieving dynamic control and polarization dependence structural color with a compact, single-layer structure.

In this work, we present a strategy to realize polarization-sensitive color generation by exploring the orientation properties of anisotropic elliptic Si nanopillars directly deposited on a Si substrate. Owning to the geometrical anisotropy, the incident white light with different polarizations was backscattered into distinct colors by anisotropic scatters. We realized the dramatic contrast of colors under two polarization states of incident light by tuning the diameters of the nanopillars along the x- and y-axes, and we experimentally obtained basic colors, such as red, green, blue, and yellow, across the visible spectrum by carefully designing the structural parameters. The calculated results showed that the color phase had only a slight variation in intensity as the viewing angle changed owning to the Mie resonance origin. Furthermore, the method suggested here can be utilized to change the output color by simple rotation of the polarizer and analyzer with efficiently and smoothly controlled structural color across the entire visible spectral range. Thus, our designed full-color anisotropic Si metasurface with the controllable and flexible generation of arbitrary polarization distributions for light paves the way toward many practical applications, such as virtual reality, ultrahigh-resolution 3D displays, and high-density information storage.

2. Methods and Materials

2.1. Sample Fabrication

The Si metasurfaces on Si wafers (100 mm diameter, prime grade, double-sided polished) were fabricated with the electron beam lithography (EBL) technique followed by inductively coupled plasma (ICP) etching. First, we cleaned the Si wafer in an ultrasound bath in acetone and anhydrous ethanol for 10 min. Second, a 150 nm PMMA (A3) film was spin-coated onto the cleaned Si wafer and baked at 180 °C for 5 min. After that, the PMMA resist was exposed to the electron beam to form the PMMA nanostructures. Then, the sample was transferred into an electron beam evaporator and directly coated with 30 nm Cr films, and then acetone was used to finally lift off the Cr mask. Then, the silicon was etched away with inductively coupled plasma (ICP) using C_3F_8 and SF_6 gases. Finally, by immersing the sample into the chromium etchant to remove the Cr, the Si metasurfaces were obtained.

2.2. Optical Characterization

The samples were assessed using an optical microscope (OLYMPUS BX51), a charge-coupled device (CCD) camera (Canon EOS 750D), and a fiber-coupled spectrometer (Ocean Optics HR4000). The structures were illuminated by a white halogen lamp (100W) and a homemade optical setup to control the polarization and incident angle. The reflection spectra were recorded by the spectrometer with a spectrometer slit size of 0.2 mm, and bright-field microscopy images were taken by the CCD camera. All reflection spectra were normalized to the reflection from an aluminum mirror.

3. Results and Discussion

The proposed structures were composed of asymmetric elliptic Si nanopillars on a Si substrate with different diameters along the x- and y-directions, as illustrated in Figure 1a. In the case of the same structure, x-polarization and y-polarization incident white light was scattered back to distinct colors due to the asymmetry of the nanopillars. The major axes and minor axes of the structure were D_x and D_y along the x- and y-directions, respectively. The lattice dimension P was fixed at 300 nm. The schematic of the single-pixel and two

top-view SEM images of typical elliptic Si nanopillar arrays are shown in the right half of Figure 1a. Figure 1b,c present a bright field optical microscope image of the fabricated elliptic Si nanopillar arrays under white light illumination through an objective of 20X (NA: 0.45). We changed the diameter of nanopillars along the x- and y-directions from 96 to 244 nm to cover the full color palette. Each area of 15 × 15 μm^2 presented an individual color corresponding to an array of nanopillars with a specific D_x and D_y. The height of the elliptic Si nanopillar was 162 nm measured by SEM. As shown in Figure 1b,c, distinct vivid color pixels of the color palette exhibited red, yellow, green, and blue. The color changed from red to blue with the increasing diameter of the nanopillar, indicating that the optical response is mainly determined by the diameter of the nanopillar. For each nanostructure group, a sharp color contrast could be obtained under the two polarized incident lights. Figure 1b shows that the color changed from red to yellow to green to blue with an increasing D_x under x-polarization, where D_y was fixed at 96 nm. For the y-polarization incidence, all pixels exhibited a distinct saturation of red. It was also possible to achieve hue- and saturation-tuned colors by varying D_x and D_y for y-polarization, as shown in Figure 1c. Particularly, we obtained a vivid blue color by simply tuning the geometric parameters of the ellipse nanopillars, which is very difficult to realize with Si nanostructures due to the higher loss of Si in the blue and violet bands.

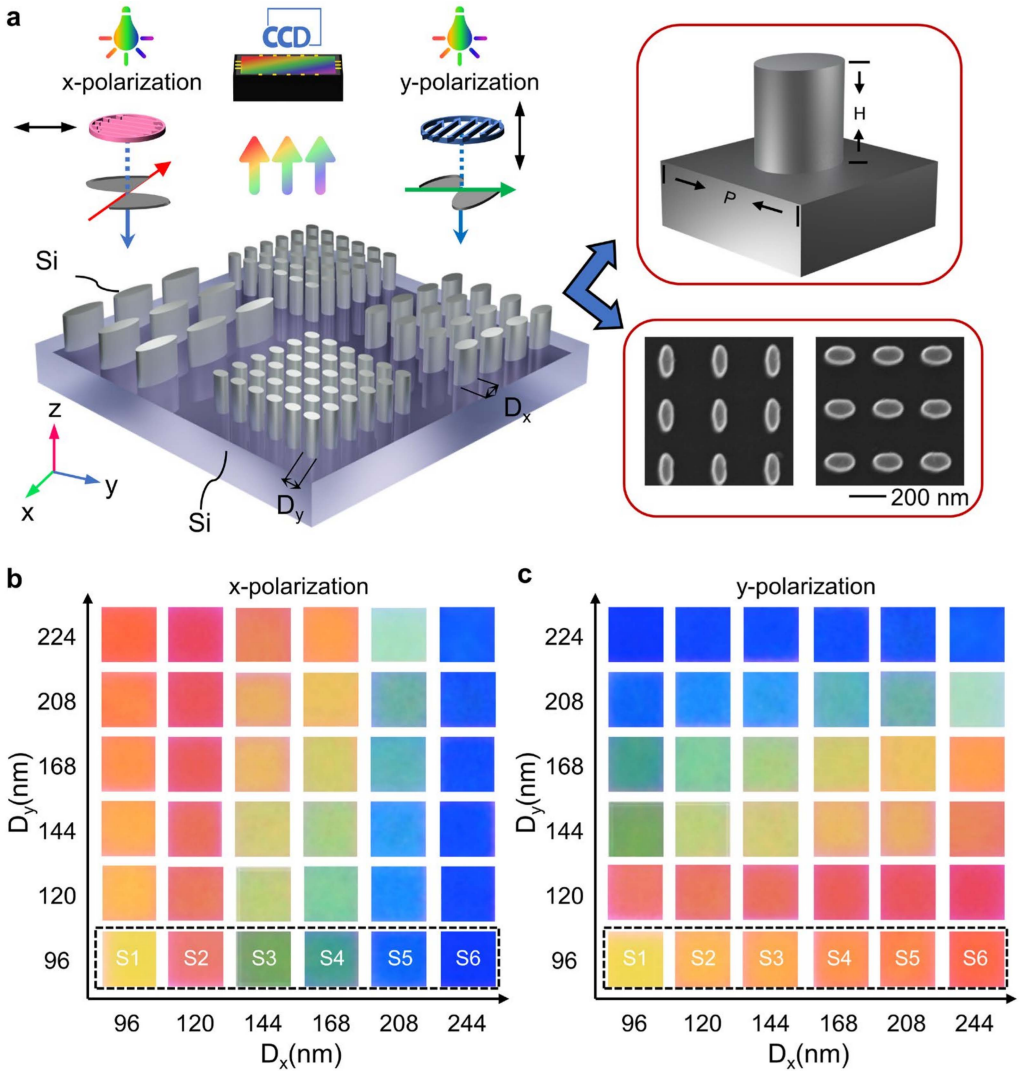

Figure 1. (**a**) Schematic of Si-based metasurfaces with periodic Si elliptical nanopillars on Si substrate. Two top-view SEM images of a typical elliptic Si nanopillar array. Optical bright microscopy image of the color palette under (**b**) x-polarization and (**c**) y-polarization light.

To analyze the reflection characteristics of the nanopillars under the x- and y-polarization states, we measured the reflection spectrums of six nanopillars under x- and y-polarization incident light, as shown in Figure 2, which correspond to the geometry parameters in the dashed box in Figure 1. For the incident light polarized along the major axis of the nanopillar, as the diameter increased, the reflection dip shifted toward longer wavelengths, and a new dip appeared at the short wavelength with a further increase in the diameter, which was determined by the period in accordance with the Rayleigh anomaly. When the nanopillars varied from S1 to S6, the main dip wavelengths of the reflected spectra were 415, 501, 539, 572, 650, and 663 nm, respectively. As a result, by simply tailoring the nanopillar size, perfect absorption of light at specific wavelengths across the visible spectrum was achieved. For the incident light polarized along the minor axis of the nanopillar, the dips in the calculated reflection spectra in Figure 2b had no apparent shift as D_x increased, which also demonstrates the modification of the saturation with a nearly unchanged hue. Given that the periods of the proposed structure in the subwavelength regime were much smaller, the slight red shift in the resonance wavelength might have been due to the near-field coupling between the adjacent nanopillars. However, the efficiency and bandwidth of the reflected spectrum were slightly different under y-polarization. We calculated the chromaticity of the colors for the x- and y- polarization incidence on the CIE 1931 color map in Figure 2c,d. The black dots in Figure 2c show that the chromaticity diagram has significantly different hues due to the presence of various main dip wavelengths, and a wide color variety can be achieved by increasing the major axis of the Si nanopillar under x- polarization incidence. By contrast, the center wavelength only moved around 10 nm; the saturation of the colors shows a slightly rising trend from S1 to S6 in Figure 2d. Therefore, we simultaneously realized the saturation- and hue-tuning structure color in two orthogonal polarization states, which is desirable for practical applications, such as anticounterfeiting, 3D display, data storage, and so on.

To illustrate the underlying mechanism of the above polarization-sensitive structural colors, we next simulated the light–matter interaction by the finite difference time domain method with periodic boundary conditions in the x- and y-directions to model infinite arrays and perfect match layers in the z-direction to mimic a free space. The refractive indices of Si were taken from the book of Edward D. Palik. It is well known that high-refractive dielectric scatters exhibit resonance when the wavelength of the incident light is similar to the physical size of the scatters and that the magnetic and electrical responses of these scatters have similar intensities. In general, the dipole mode resonance wavelength of nanostructures in air is $\lambda/n \sim d$, and when the diameter is large enough, the nanostructures also support higher-order modes in the visible spectrum. We present the magnetic field distributions of S3 at the resonant wavelength of A at 432 nm and B at 539 nm under x- and y-polarization states in Figure 3. Figure 3a,b show the magnetic field distributions $|H|$ in the x–z plane at wavelengths of 432 nm under two polarization states. Figure 3c,d show $|H|$ at wavelengths of 539 nm under two polarization states. All the magnetic field distributions at resonant wavelength were the strongest at the center of the nanopillar in view of the observed field profiles. In general, magnetic dipole resonance with high absorption and minimal scattering compared with an electric dipole at resonances with longer wavelengths, we found that some of the energy leaked into the substrate, and they could decrease the resonant reflection and form a deep resonant dip. The magnetic field distribution was weak and primarily located in the interior of the Si nanopillar for the non-resonant wavelength, as shown in Figure 3a,d. The above phenomenon indicates that the resonance mechanism of the two polarization states is identical. It depends on the inherent properties of Si; the periodic arrangement of Si nanopillars can support dipole resonance and form channels that can introduce light energy to the Si substrate, deepening the dip of the reflection spectrum.

We also investigated the angle independence of the anisotropic metasurface designed on the basis of Si elliptic nanopillars. In order to investigate how the angle of view affects the structural color through reflectance, we calculated the periodic structural reflection spectra of D_x = 120 nm and D_y = 96 nm under x- and y-polarization states, respectively,

in Figure 4a,c. The reflection efficiency was a function of the incidence angle and wavelength. For x- and y-polarizations, the central resonant positions were 490 nm and 435 nm, respectively, and they remained nearly constant, with only a slight variation in intensity from 0 to 30° as the angle of incidence changed. As a result, color hardly changed with increasing incidence angles, and color phase remained almost constant on the CIE 1931 diagrams when the incident angle was less than 30°, as shown in Figure 4b,d. However, when the incidence angle of the light was greater than 30°, the view angle change of the structural color was slightly different for the x- and y-polarization. For the x-polarization, when the incident angle was greater than 30°, there was a specific resonance around the main resonant dip, which gradually grew. The reflected light became less monochromatic, resulting in a decrease in saturation, so the color changed from magenta to deep orange to brownish yellow. At the same time, under the y-polarization, with an increase in the incident angle, the position of the resonance dip remained almost unchanged. When the incidence angle was greater than 50°, the reflection increased precipitously to nearly 600 nm, so the color changed from orange to yellow.

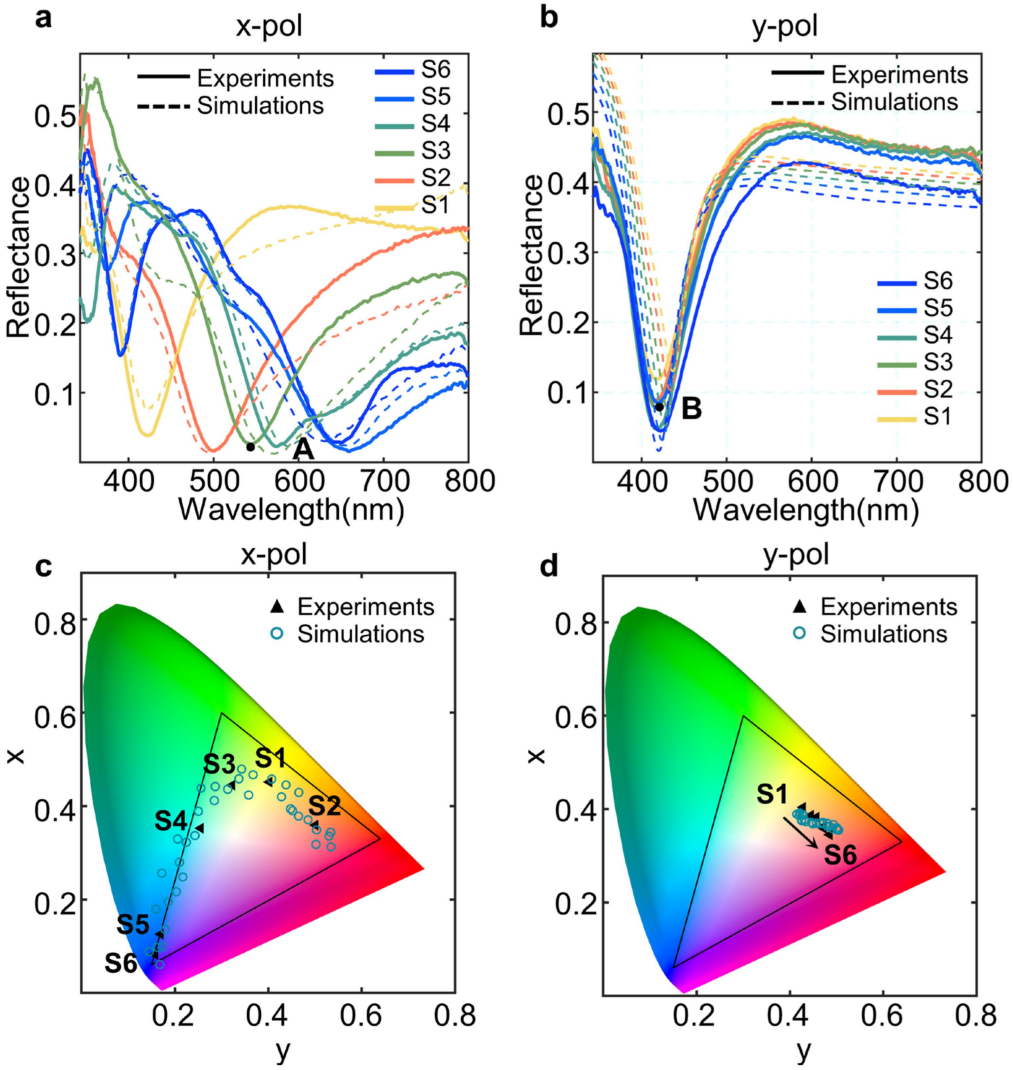

Figure 2. Simulated and experimental reflection spectra under (**a**) x- and (**b**) y-polarization light. Corresponding CIE 1931 chromaticity coordinates for (**c**) x- and (**d**) y-polarization, respectively.

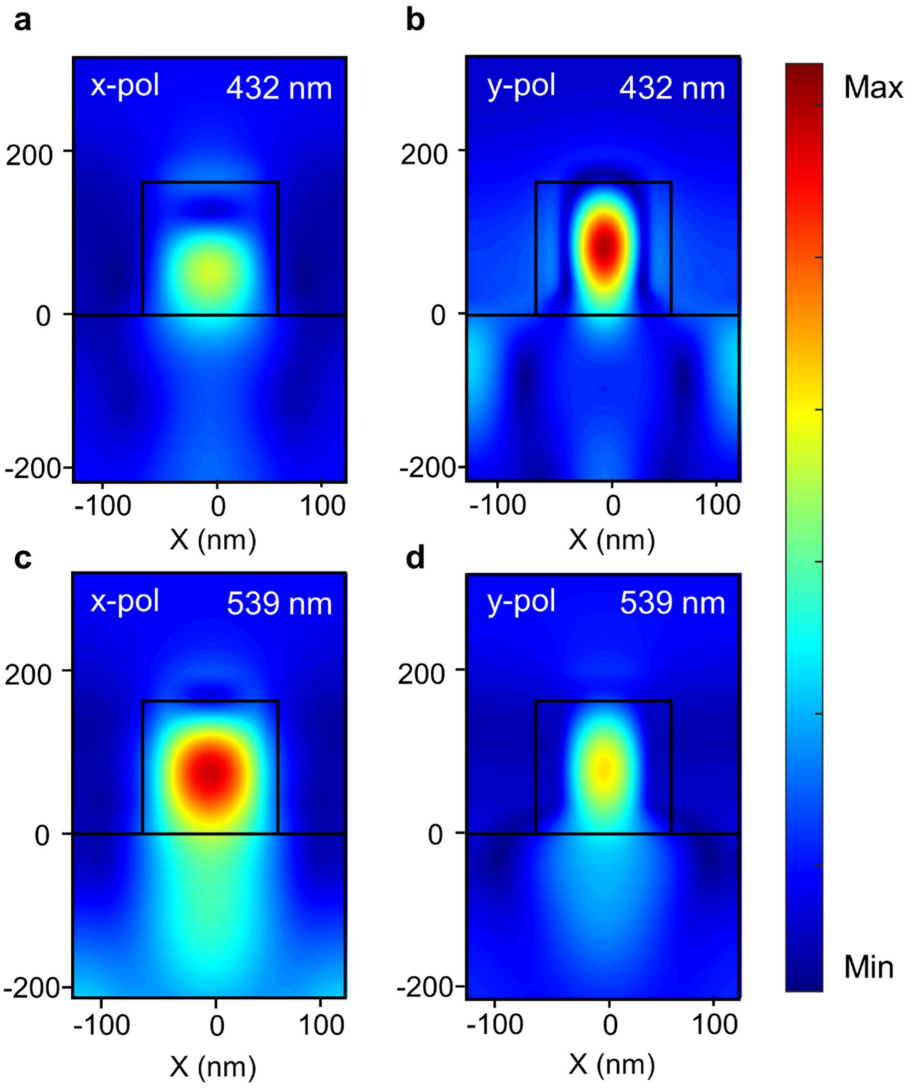

Figure 3. Simulated magnetic field distributions |H| in x–z plane at resonant wavelength of 432 nm under (**a**) x-polarization and (**b**) y-polarization, respectively, and at resonant wavelength of 539 nm under (**c**) x-polarization and (**d**) y-polarization, respectively.

Figure 4e shows a simulated color image with an equivalent hue at a 10° interval of oblique incident light. The color under two polarization states remained basically constant from 0° to 30°, which was consistent with the results in Figure 4a,c. In accordance with the visual field of a single human eye, the symbol recognition angle was about 30°, so our Si nanostructure color perspective independence is suitable for small-angle display applications. In addition, it can be used for wide-angle detectors and angle-sensitive microscopes due to the great change in color saturation with a varying incident angle when the incident angle is greater than 30°.

The designed elliptical Si nanostructure possesses strong anisotropy so that we can establish a polarization-controlled structural color generation mechanism by changing its polarization state. The proposed elliptical Si metasurfaces have different colors under different observation conditions. To investigate the basic working process of manipulating the polarization, various combinations of the input polarizer and output analyzer angle differences (φ_p—φ_a) were utilized. According to Malus's law, the output intensity of reflection through a polarizer and analyzer depends on the relative angle between the polarization axis of the polarizer and the electric field orientation of the reflected light. Figure 5 shows the measured reflection spectra for different settings of the input polarization angle ($\varphi_p = 0°$, 45°, 90°, and 135°) as a function of the output analyzer angle

($0° < \varphi_a < 360°$, in steps of 1°). For the $\varphi_p = 0°$ and 90° states, the reflection was blocked if the analyzing polarizer had incident polarization. Thus, if $\varphi_p = \varphi_a$, the reflection was at a maximum, and if φ_p was at a right angle to the φ_a, the reflection was zero, as shown in Figure 5b,f. When the input polarization angles were 45° and 135°, the situation was more intricate. Each elliptical nanopillar can generate two independent phase shifts of reflected light in two directions. Very different colors were thus obtained for different settings of the analyzing polarizer (φ_a). Figure 5d,h show that the reflection spectra sensitively depend on the setting of φ_a. The maxima shifted as φ_a was altered, but the overall intensities were preserved, which clearly indicated a phase shift. In the diagonal case ($\varphi_p = 45°$ and 135°), the phase shift was responsible for the observation of four separate output colors, and only a single color was observed for each x-polarization and y-polarization ($\varphi_p = 0°$ and 90°).

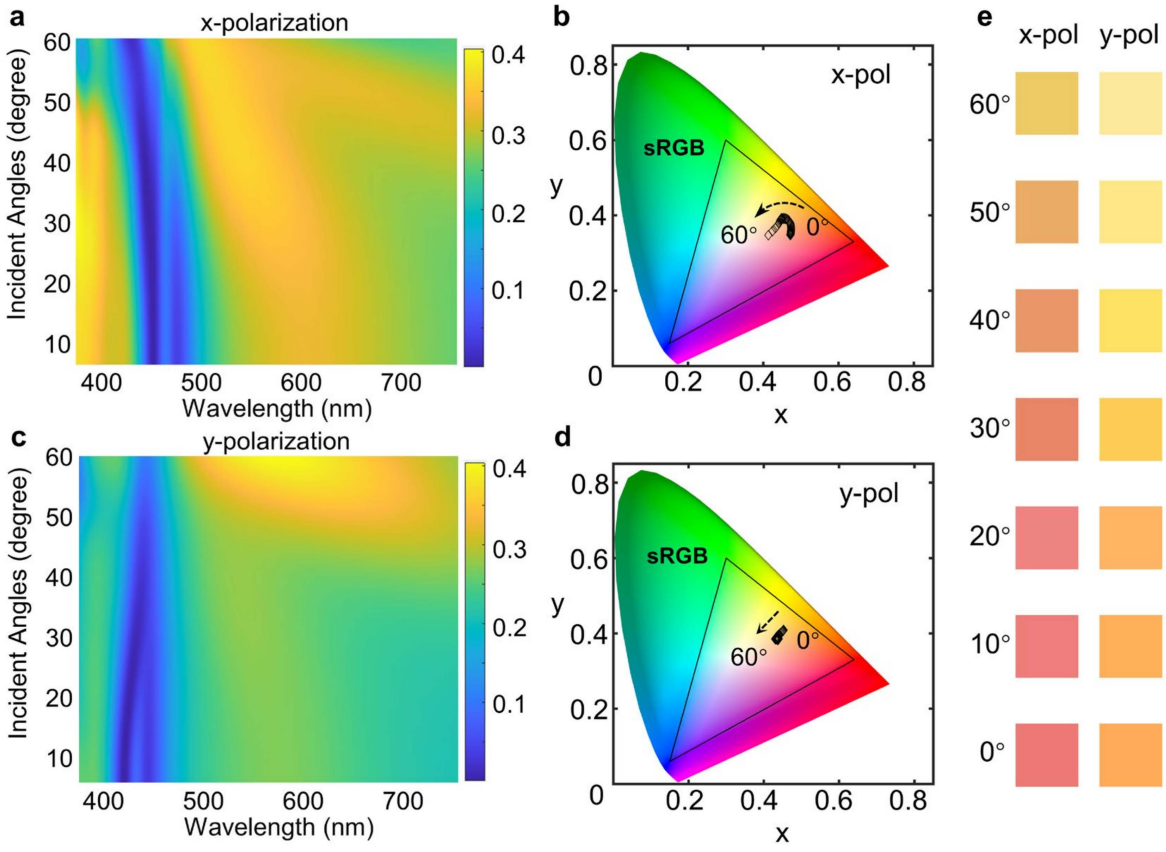

Figure 4. Simulated reflection spectra of S2 (D_x = 120 nm, D_y = 96 nm) under (**a**) x- and (**c**) y-polarization. Corresponding CIE 1931 chromaticity coordinates under (**b**) x- and (**d**) y-polarization. (**e**) Corresponding colors for varying incident angles from 0° to 90° with 10° interval.

As a result, the input linear polarization light (45° with respect to the long axis of the elliptical nanopillar) was converted into elliptical polarized states. This color dependence on the polarization angle is particularly useful, leading to the dynamic control of the color by changing the polarization angle of the incident light and output light, which can be used in 3D displaying and high-density storage and is essential for encryption and anticounterfeiting.

Corresponding CIE 1931 chromaticity coordinates of the reflection spectra in Figure 5b,d are shown in Figure 6. When the polarizer was orientated at 0°, which corresponded to the x-polarization incident light, the corresponding color hue was unchanged, and only the brightness changed with a varying analyzer angle. When the input polarization angle was 45°, the colors showed a very strong contrast with varying analyzer angles. These appear in Figure 5c as purple, dark blue, brown, and dark green.

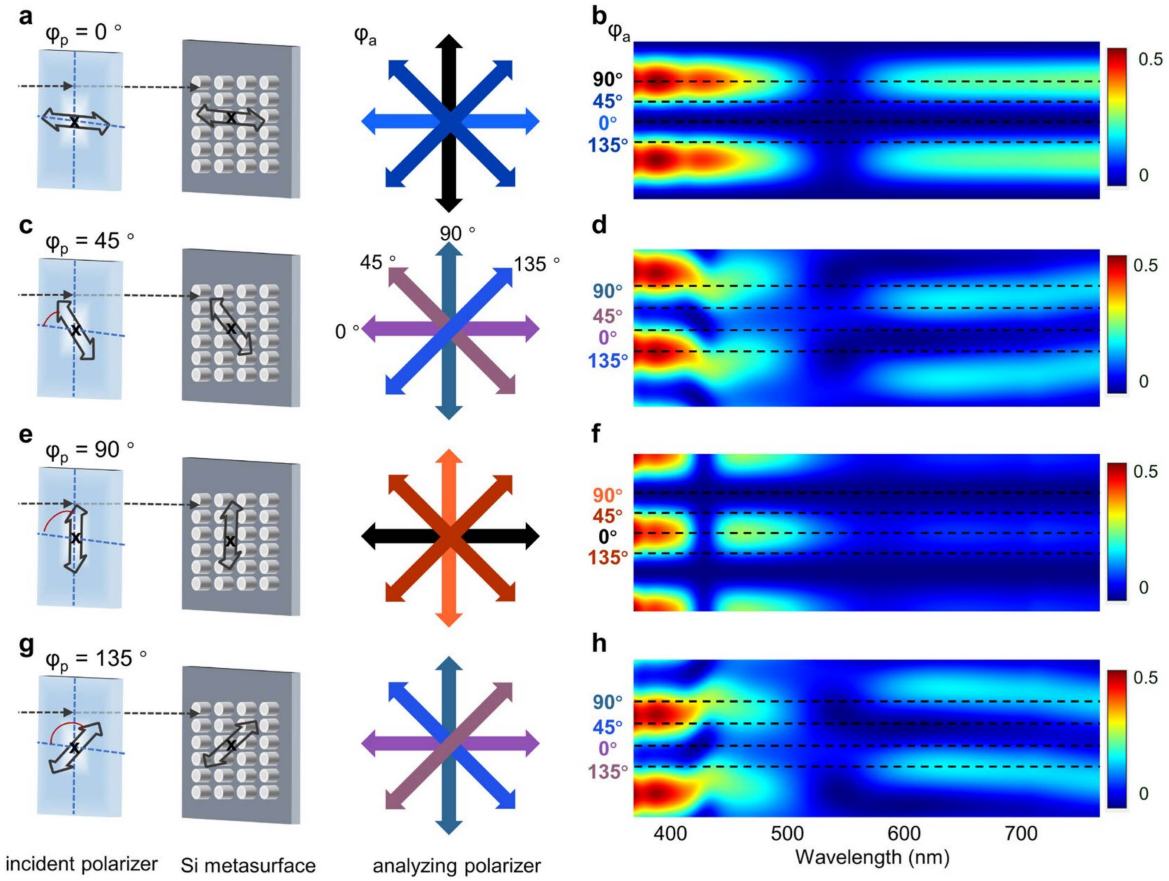

Figure 5. Reflection spectra as a function of polarization angles. (**a**,**c**,**e**,**g**) Measurement schemes for different angles of the incident polarizer (φ_p) and the analyzing polarizer (φ_a); each output arrow is colored in the observed color. (**b**,**d**,**f**,**h**) Corresponding calculated reflection plots for rotation of the analyzing polarizer ($0^\circ < \theta < 360^\circ$, 1° steps).

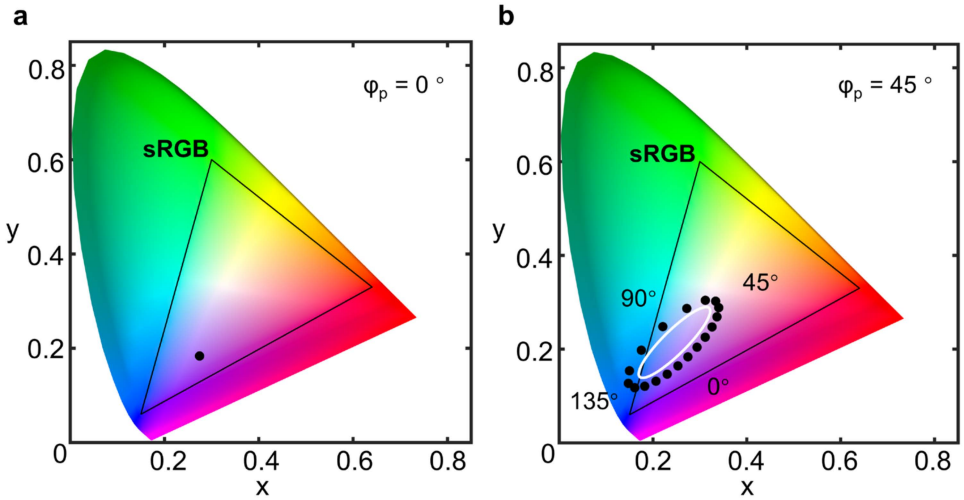

Figure 6. Corresponding CIE 1931 chromaticity coordinates of the reflection spectra in (**a**) Figure 5d and (**b**) Figure 5f.

4. Conclusions

In conclusion, we demonstrated polarization-sensitive structural colors based on anisotropic metasurfaces consisting of elliptical Si nanopillar arrays directly on a Si substrate, which generate colors using Mie resonances confined in Si nanopillars. Regular colors, such as red, green, blue, and yellow, across the visible spectrum were generated by

simply tuning the axis of elliptical nanopillars. A distinct feature of our design is that the pixel preserves the color phase independently of the viewing angle, which is fundamental for real applications. More importantly, multiple colors can be obtained by changing the polarizer and analyzer angles. Our proposed metasurface has a lower cost and is more compatible with standard CMOS technology, holding great potential for many practical applications, such as virtual reality, ultrahigh-resolution 3D displays, and high-density information storage.

Author Contributions: Conceptualization, X.S.; methodology, X.S. and L.S.; software, X.S., H.L., L.L. and H.H.; validation, X.S., H.H., C.L. and J.N.; formal analysis, X.S. and L.L.; resources, H.H. and C.L.; writing—original draft preparation, X.S.; writing—review and editing, X.S. and L.S.; supervision, X.S. and H.L.; funding acquisition, L.S. All authors have read and agreed to the published version of the manuscript.

Funding: This research was funded by the National Key R&D Program of China 2019YFB2205002, the National Natural Science Foundation of China (Grant No. 61875225, 61888102). The APC was funded by the National Natural Science Foundation of China (Grant No. 61875225).

Institutional Review Board Statement: Not applicable.

Informed Consent Statement: Not applicable.

Data Availability Statement: Not applicable.

Conflicts of Interest: The authors declare no conflict of interest.

References

1. Vukusic, P.; Sambles, J.R. Photonic structures in biology. *Nature* **2003**, *424*, 852–855. [CrossRef] [PubMed]
2. Rouw, R.; Scholte, H.S. Increased structural connectivity in grapheme-color synesthesia. *Nat. Neurosci.* **2007**, *10*, 792–797. [CrossRef] [PubMed]
3. Bohren, C.F.; Huffman, D.R. *Absorption and Scattering of Light by Small Particles*; John Wiley & Sons: Hoboken, NJ, USA, 2008.
4. Kerker, M. *The Scattering of Light and Other Electromagnetic Radiation*; Elsevier: Amsterdam, The Netherlands, 2016.
5. Brown, M.A.; De Vito, S.C. Predicting azo dye toxicity. *Crit. Rev. Environ. Sci. Technol.* **1993**, *23*, 249–324. [CrossRef]
6. Baek, K.; Kim, Y.; Mohd-Noor, S.; Hyun, J.K. Mie Resonant Structural Colors. *ACS Appl. Mater. Interfaces* **2020**, *12*, 5300–5318. [CrossRef] [PubMed]
7. Kinoshita, S.; Yoshioka, S.; Miyazaki, J. Physics of structural colors. *Rep. Prog. Phys.* **2008**, *71*, 076401. [CrossRef]
8. Shen, Y.; Rinnerbauer, V.; Wang, I.; Stelmakh, V.; Joannopoulos, J.D.; Soljačić, M. Structural Colors from Fano Resonances. *ACS Photonics* **2015**, *2*, 27–32. [CrossRef]
9. Song, M.; Wang, D.; Peana, S.; Choudhury, S.; Nyga, P.; Kudyshev, Z.A.; Yu, H.; Boltasseva, A.; Shalaev, V.M.; Kildishev, A.V. Colors with plasmonic nanostructures: A full-spectrum review. *Appl. Phys. Rev.* **2019**, *6*, 041308. [CrossRef]
10. Tittl, A. Tunable structural colors on display. *Light Sci. Appl.* **2022**, *11*, 155. [CrossRef]
11. Yang, B.; Cheng, H.; Chen, S.; Tian, J. Structural colors in metasurfaces: Principle, design and applications. *Mater. Chem. Front.* **2019**, *3*, 750–761. [CrossRef]
12. Yang, W.; Xiao, S.; Song, Q.; Liu, Y.; Wu, Y.; Wang, S.; Yu, J.; Han, J.; Tsai, D.P. All-dielectric metasurface for high-performance structural color. *Nat. Commun.* **2020**, *11*, 1864. [CrossRef]
13. Zhao, Y.; Xie, Z.; Gu, H.; Zhu, C.; Gu, Z.J.C.S.R. Bio-inspired variable structural color materials. *Chem. Soc. Rev.* **2012**, *41*, 3297–3317. [CrossRef] [PubMed]
14. Van de Groep, J.; Polman, A. Designing dielectric resonators on substrates: Combining magnetic and electric resonances. *Opt. Express* **2013**, *21*, 26285–26302. [CrossRef] [PubMed]
15. Hentschel, M.; Koshelev, K.; Sterl, F.; Both, S.; Karst, J.; Shamsafar, L.; Weiss, T.; Kivshar, Y.; Giessen, H. Dielectric Mie voids: Confining light in air. *Light Sci. Appl.* **2023**, *12*, 3. [CrossRef] [PubMed]
16. Xu, T.; Wu, Y.-K.; Luo, X.; Guo, L.J. Plasmonic nanoresonators for high-resolution colour filtering and spectral imaging. *Nat. Commun.* **2010**, *1*, 59. [CrossRef]
17. Cheng, F.; Gao, J.; Luk, T.S.; Yang, X. Structural color printing based on plasmonic metasurfaces of perfect light absorption. *Sci. Rep.* **2015**, *5*, 11045. [CrossRef]
18. Cheng, F.; Gao, J.; Stan, L.; Rosenmann, D.; Czaplewski, D.; Yang, X. Aluminum plasmonic metamaterials for structural color printing. *Opt. Express* **2015**, *23*, 14552–14560. [CrossRef]
19. Dai, Q.; Zhu, G.; Zhang, W.; Li, J.; Li, Z.; Cui, H.; Wei, K.; He, Z.; Guan, Z.; Zheng, G. Dual-channel anticounterfeiting color-nanoprinting with a single-size nanostructured metasurface. *Opt. Express* **2022**, *30*, 33574–33587. [CrossRef]
20. Dong, Z.; Ho, J.; Yu, Y.F.; Fu, Y.H.; Paniagua-Dominguez, R.; Wang, S.; Kuznetsov, A.I.; Yang, J.K.W. Printing Beyond sRGB Color Gamut by Mimicking Silicon Nanostructures in Free-Space. *Nano Lett.* **2017**, *17*, 7620–7628. [CrossRef]

21. Kumar, K.; Duan, H.; Hegde, R.S.; Koh, S.C.W.; Wei, J.N.; Yang, J.K.W. Printing colour at the optical diffraction limit. *Nat. Nanotechnol.* **2012**, *7*, 557–561. [CrossRef]
22. Liu, X.; Huang, Z.; Zang, J. All-Dielectric Silicon Nanoring Metasurface for Full-Color Printing. *Nano Lett.* **2020**, *20*, 8739–8744. [CrossRef]
23. Miyata, M.; Hatada, H.; Takahara, J. Full-Color Subwavelength Printing with Gap-Plasmonic Optical Antennas. *Nano Lett.* **2016**, *16*, 3166–3172. [CrossRef] [PubMed]
24. Nagasaki, Y.; Hotta, I.; Suzuki, M.; Takahara, J. Metal-Masked Mie-Resonant Full-Color Printing for Achieving Free-Space Resolution Limit. *ACS Photonics* **2018**, *5*, 3849–3855. [CrossRef]
25. Nagasaki, Y.; Suzuki, M.; Hotta, I.; Takahara, J. Control of Si-Based All-Dielectric Printing Color through Oxidation. *ACS Photonics* **2018**, *5*, 1460–1466. [CrossRef]
26. Sun, S.; Zhou, Z.; Zhang, C.; Gao, Y.; Duan, Z.; Xiao, S.; Song, Q. All-dielectric full-color printing with TiO_2 metasurfaces. *ACS Nano* **2017**, *11*, 4445–4452. [CrossRef]
27. Tan, S.J.; Zhang, L.; Zhu, D.; Goh, X.M.; Wang, Y.M.; Kumar, K.; Qiu, C.-W.; Yang, J.K.W. Plasmonic Color Palettes for Photorealistic Printing with Aluminum Nanostructures. *Nano Lett.* **2014**, *14*, 4023–4029. [CrossRef] [PubMed]
28. Zhang, Y.; Zhang, Q.; Ouyang, X.; Lei, D.Y.; Zhang, A.P.; Tam, H.-Y. Ultrafast Light-Controlled Growth of Silver Nanoparticles for Direct Plasmonic Color Printing. *ACS Nano* **2018**, *12*, 9913–9921. [CrossRef]
29. Shang, X.; Niu, J.; Wang, C.; Li, L.; Lu, C.; Zhang, Y.; Shi, L. Mie Resonances Enabled Subtractive Structural Colors with Low-Index-Contrast Silicon Metasurfaces. *ACS Appl. Mater. Interfaces* **2022**, *14*, 55933–55943. [CrossRef]
30. Li, L.; Niu, J.; Shang, X.; Chen, S.; Lu, C.; Zhang, Y.; Shi, L. Bright Field Structural Colors in Silicon-on-Insulator Nanostructures. *ACS Appl. Mater. Interfaces* **2021**, *13*, 4364–4373. [CrossRef]
31. Shi, L.; Niu, J.; Li, L.; Wang, C.; Shang, X.; Zhang, P.; Liu, Y.; Zhang, Y. Deep Subwavelength Wide-Angle Structural Colors at the Single Pixel Level. *Adv. Opt. Mater.* **2022**, *10*, 2200552. [CrossRef]
32. Shi, S.; Lu, H.; Li, Y.; Bo, S.; Li, D.; Zhao, J. Asymmetric nanocavities with wide reflection color gamut for color printing. *Nanotechnology* **2022**, *34*, 025201. [CrossRef]
33. Liu, H.; Wang, H.; Wang, H.; Deng, J.; Ruan, Q.; Zhang, W.; Abdelraouf, O.A.; Ang, N.S.S.; Dong, Z.; Yang, J.K. High-Order Photonic Cavity Modes Enabled 3D Structural Colors. *ACS Nano* **2022**, *16*, 8244–8252. [CrossRef] [PubMed]
34. Hu, T.; Tseng, C.K.; Fu, Y.H.; Xu, Z.; Dong, Y.; Wang, S.; Lai, K.H.; Bliznetsov, V.; Zhu, S.; Lin, Q.; et al. Demonstration of color display metasurfaces via immersion lithography on a 12-inch silicon wafer. *Opt. Express* **2018**, *26*, 19548–19554. [CrossRef] [PubMed]
35. Joo, W.J.; Kyoung, J.; Esfandyarpour, M.; Lee, S.H.; Koo, H.; Song, S.; Kwon, Y.N.; Song, S.H.; Bae, J.C.; Jo, A.; et al. Metasurface-driven OLED displays beyond 10,000 pixels per inch. *Science* **2020**, *370*, 459–463. [CrossRef] [PubMed]
36. Olson, J.; Manjavacas, A.; Basu, T.; Huang, D.; Schlather, A.E.; Zheng, B.; Halas, N.J.; Nordlander, P.; Link, S. High Chromaticity Aluminum Plasmonic Pixels for Active Liquid Crystal Displays. *ACS Nano* **2016**, *10*, 1108–1117. [CrossRef]
37. Song, M.; Li, X.; Pu, M.; Guo, Y.; Liu, K.; Yu, H.; Ma, X.; Luo, X. Color display and encryption with a plasmonic polarizing metamirror. *Nanophotonics* **2018**, *7*, 323–331. [CrossRef]
38. Xu, G.; Kang, Q.; Fan, X.; Yang, G.; Guo, K.; Guo, Z. Influencing Effects of Fabrication Errors on Performances of the Dielectric Metalens. *Micromachines* **2022**, *13*, 2098. [CrossRef] [PubMed]
39. Wang, W.; Zhao, R.; Chang, S.; Li, J.; Shi, Y.; Liu, X.; Sun, J.; Kang, Q.; Guo, K.; Guo, Z. High-efficiency spin-related vortex metalenses. *Nanomaterials* **2021**, *11*, 1485. [CrossRef]
40. Wang, W.; Yang, Q.; He, S.; Shi, Y.; Liu, X.; Sun, J.; Guo, K.; Wang, L.; Guo, Z. Multiplexed multi-focal and multi-dimensional SHE (spin Hall effect) metalens. *Opt. Express* **2021**, *29*, 43270–43279. [CrossRef]
41. Song, M.; Wang, D.; Kudyshev, Z.A.; Xuan, Y.; Wang, Z.; Boltasseva, A.; Shalaev, V.M.; Kildishev, A.V. Enabling Optical Steganography, Data Storage, and Encryption with Plasmonic Colors. *Laser Photonics Rev.* **2021**, *15*, 2000343. [CrossRef]
42. Heydari, E.; Sperling, J.R.; Neale, S.L.; Clark, A.W. Plasmonic Color Filters as Dual-State Nanopixels for High-Density Microimage Encoding. *Adv. Funct. Mater.* **2017**, *27*, 1701866. [CrossRef]
43. Shrestha, V.R.; Lee, S.S.; Kim, E.S.; Choi, D.Y. Aluminum plasmonics based highly transmissive polarization-independent subtractive color filters exploiting a nanopatch array. *Nano Lett.* **2014**, *14*, 6672–6678. [CrossRef] [PubMed]
44. Raj Shrestha, V.; Lee, S.-S.; Kim, E.-S.; Choi, D.-Y. Polarization-tuned dynamic color filters incorporating a dielectric-loaded aluminum nanowire array. *Sci. Rep.* **2015**, *5*, 12450. [CrossRef] [PubMed]
45. Balaur, E.; Sadatnajafi, C.; Kou, S.S.; Lin, J.; Abbey, B. Continuously Tunable, Polarization Controlled, Colour Palette Produced from Nanoscale Plasmonic Pixels. *Sci. Rep.* **2016**, *6*, 28062. [CrossRef] [PubMed]
46. Li, Z.; Clark, A.W.; Cooper, J.M. Dual color plasmonic pixels create a polarization controlled nano color palette. *ACS Nano* **2016**, *10*, 492–498. [CrossRef] [PubMed]
47. Vashistha, V.; Vaidya, G.; Gruszecki, P.; Serebryannikov, A.E.; Krawczyk, M. Polarization tunable all-dielectric color filters based on cross-shaped Si nanoantennas. *Sci. Rep.* **2017**, *7*, 8092. [CrossRef]
48. Yang, B.; Liu, W.; Li, Z.; Cheng, H.; Chen, S.; Tian, J. Polarization-Sensitive Structural Colors with Hue-and-Saturation Tuning Based on All-Dielectric Nanopixels. *Adv. Opt. Mater.* **2018**, *6*, 1701009. [CrossRef]
49. Zang, X.; Dong, F.; Yue, F.; Zhang, C.; Xu, L.; Song, Z.; Chen, M.; Chen, P.Y.; Buller, G.S.; Zhu, Y.; et al. Polarization Encoded Color Image Embedded in a Dielectric Metasurface. *Adv. Mater.* **2018**, *30*, e1707499. [CrossRef]

50. Gao, S.; Park, C.S.; Lee, S.S.; Choi, D.Y. All-dielectric metasurfaces for simultaneously realizing polarization rotation and wavefront shaping of visible light. *Nanoscale* **2019**, *11*, 4083–4090. [CrossRef]
51. Fan, J.; Cheng, Y. Broadband high-efficiency cross-polarization conversion and multi-functional wavefront manipulation based on chiral structure metasurface for terahertz wave. *J. Phys. D Appl. Phys.* **2020**, *53*, 025109. [CrossRef]
52. Jung, C.; Yang, Y.; Jang, J.; Badloe, T.; Lee, T.; Mun, J.; Moon, S.-W.; Rho, J. Near-zero reflection of all-dielectric structural coloration enabling polarization-sensitive optical encryption with enhanced switchability. *Nanophotonics* **2020**, *10*, 919–926. [CrossRef]
53. Yue, W.; Gao, S.; Li, Y.; Zhang, C.; Fu, X.; Choi, D.-Y. Polarization-encrypted high-resolution full-color images exploiting hydrogenated amorphous silicon nanogratings. *Nanophotonics* **2020**, *9*, 875–884. [CrossRef]
54. Zhang, C.; Jing, J.; Wu, Y.; Fan, Y.; Yang, W.; Wang, S.; Song, Q.; Xiao, S. Stretchable All-Dielectric Metasurfaces with Polarization-Insensitive and Full-Spectrum Response. *ACS Nano* **2020**, *14*, 1418–1426. [CrossRef] [PubMed]
55. Zhao, J.; Yu, X.; Zhou, K.; Zhang, W.; Yuan, W.; Yu, Y. Polarization-sensitive subtractive structural color used for information encoding and dynamic display. *Opt. Lasers Eng.* **2021**, *138*, 106421. [CrossRef]
56. Guo, X.; Zhong, J.; Li, B.; Qi, S.; Li, Y.; Li, P.; Wen, D.; Liu, S.; Wei, B.; Zhao, J. Full-Color Holographic Display and Encryption with Full-Polarization Degree of Freedom. *Adv. Mater.* **2022**, *34*, e2103192. [CrossRef] [PubMed]
57. Guo, K.; Li, X.; Ai, H.; Ding, X.; Wang, L.; Wang, W.; Guo, Z. Tunable oriented mid-infrared wave based on metasurface with phase change material of GST. *Results Phys.* **2022**, *34*, 105269. [CrossRef]
58. Kang, Q.; Li, D.; Wang, W.; Guo, K.; Guo, Z. Multiband tunable thermal camouflage compatible with laser camouflage based on GST plasmonic metamaterial. *J. Phys. D Appl. Phys.* **2021**, *55*, 065103. [CrossRef]
59. Ai, H.; Kang, Q.; Wang, W.; Guo, K.; Guo, Z. Multi-beam steering for 6G communications based on graphene metasurfaces. *Sensors* **2021**, *21*, 4784. [CrossRef]
60. Kang, Q.; Li, D.; Guo, K.; Gao, J.; Guo, Z. Tunable thermal camouflage based on GST plasmonic metamaterial. *Nanomaterials* **2021**, *11*, 260. [CrossRef]
61. Ding, X.; Kang, Q.; Guo, K.; Guo, Z. Tunable GST metasurfaces for chromatic aberration compensation in the mid-infrared. *Opt. Mater.* **2020**, *109*, 110284. [CrossRef]
62. Moon, J.-B.; Lee, S.-J.; Kim, S.-H.; Chang, Y.; Hwang, H.; Yi, G.-R. Mie-Resonant Rutile TiO_2 Nanospheres for Unclonable Structural Colors. *Chem. Mater.* **2022**, *34*, 7897–7905. [CrossRef]
63. Xu, T.; Walter, E.C.; Agrawal, A.; Bohn, C.; Velmurugan, J.; Zhu, W.; Lezec, H.J.; Talin, A.A. High-contrast and fast electrochromic switching enabled by plasmonics. *Nat. Commun.* **2016**, *7*, 10479. [CrossRef] [PubMed]